Delamination migration in multidirectional composite laminates under mode I quasi-static and fatigue loading

Yu Gong[a, b,c, *], Bing Zhang[b], Stephen R. Hallett[b]

[a] College of Aerospace Engineering, Chongqing University, Chongqing 400044, China

[b] Bristol Composites Institute (ACCIS), University of Bristol, Queen's Building, University Walk, Bristol BS8 1TR, UK

[c] School of Astronautics, Beihang University, Beijing 100191, China

Abstract:

Delamination migration is particularly critical in multi-directional composite laminates and is often observed in different loading scenarios and components. Further understanding on the migration mechanism, especially the similarities and differences in the quasi-static and fatigue delamination migrations, is important for the design of composite structures. In this study, the process of delamination migration under mode I quasi-static and fatigue loadings was experimentally investigated for specimens with a +θ/-θ centreline interface. Specimens, with a specially designed stacking sequence, which allows migration events using a simple Double Cantilever Beam set-up, were tested for θ=75^o and 60^o. Delamination migration via intralaminar ply splitting has been observed and this was confirmed by the X-ray computed tomography scan results. All the specimens from both quasi-static and fatigue loadings had a fairly similar sequence of damage events; delamination grows through the –θ and +θ ply block successively until it reaches the 0^o ply that prevents further migration. The delamination paths and shape of fracture surfaces were observed to be the same, while the Scanning Electron Microscope fractography results showed that the quasi-static fracture surface was rougher in comparison with that of fatigued specimens. In addition, the distances of migration points from the pre-crack tip were slightly smaller in the fatigue specimens, which may indicate a greater propensity for migration under fatigue loading. This study provides important guidelines to the damage tolerance design of multidirectional composite

* Corresponding author: Yu Gong, E-mail: gongyu@buaa.edu.cn

structures and the verification of advanced numerical modelling technologies.

***Keywords*:** Carbon fibre; Delamination; Transverse cracking; Mechanical testing

1 Introduction

Delamination is considered one of the most critical failure modes in widely used high-performance laminated composites [1-5]. Multidirectional laminates are usually applied in real structures, considering their tailoring ability for in-plane mechanical properties. Delamination growth in multidirectional laminates commonly involves multiple delamination cracks, which often grow and migrate into different ply interfaces via matrix cracking. Thus delamination does not always remain at the initial plane for multidirectional laminates [6], which is not typical in the usual delamination characterisation testing. Delamination migration is considered to be the result of coalescence of a series of angled microcracks that develop ahead of the crack tip with an orientation perpendicular to the resolved tensile stress [7]. These microcracks accumulate and grow out-of-plane, until reaching a favorable interlaminar interface. The migration phenomenon brings about difficulties in characterisation of the fracture toughness of multidirectional laminates using conventional testing standards [8, 9], which were designed for unidirectional laminates with a single delamination. Several approaches have been proposed to suppress delamination migration. For instance, Robinson et al. [10] designed a specimen for testing of multi-directional laminates, which was different from the conventional Double Cantilever Beam (DCB) specimen due to the introduction of edge delaminations through the use of Teflon inserts. However, it did not always ensure co-planar delamination growth [11], which made it more difficult to measure true crack tip position. Another approach that has been adopted is to use an asymmetric DCB specimen, where desirable crack propagation behaviour was obtained, with no change of delamination plane [12]. The migration event is more generally difficult to suppress, as it can be initiated by various loading

scenarios; e.g. low-velocity impact [13], debonding between the flange and skin of integrally stiffened panels [14], tensile loading applied to composites with embedded defects and notches [15-18] and shear loading in non-unidirectional laminates [19-23]. These examples highlight that knowledge of single-interface delamination growth is not sufficient for a complete understanding of real applications. A lack of understanding of the migration mechanisms may potentially limit the use of composite laminates in aerospace structures. Therefore, it is critically important to establish a deeper knowledge of the fundamental driving mechanisms for delamination migration at multidirectional ply interfaces.

Several researchers have clearly documented the observed migration behaviour, but the results may not be suitable for migration criteria evaluation since the precise condition under which delamination migration initiates is difficult to pinpoint, due to multiple damage events occuring. Limited experimental work has been carried out to specifically study delamination migration in laminates. Ratcliffe et al. [24] designed a set-up capable of isolating a single complete migration event after the delamination growth onset. The studied cross-ply specimen allows an approximately two-dimensional characterisation of a uniform migration event across the specimen width. However, one issue with the test was that delamination growth onset and migration tend to be unstable. Hence a modification on the stacking sequence was conducted in order to promote stable delamination growth and migration [25]. The above mentioned cross-ply specimen is excellent for academic research but has more limited practical application. With regard to other more general stacking sequences, Pernice et al. [26] investigated delamination migration at the $0^o/60^o$ and $0^o/75^o$ interfaces, whereby finite element analysis was applied to qualitatively interpret experimental results, based on the shear stress sign at the delamination front. Studies throughout the open literatures mainly

focused on delamination migration under quasi-static loading, and the delamination migration mechanisms under fatigue loading have not yet been investigated. Fatigue loading and potential failure are recently receiving more attention, since aircraft structures are bearing more severe service loads. The study of delamination migration therefore needs to be expanded into the fatigue loading regime.

The motivation of this paper, thus, is to obtain better understanding on migration mechanisms under quasi-static and fatigue loading, especially the similarities and differences between these two loading cases. To this end, this paper describes an experimental testing programme on specimens with +θ/-θ centreline interfaces. A specific stacking sequence was designed to reduce tension/bending//twisting coupling effects, and migration event was investigated using a simple DCB set-up. Images of the delamination and migration events were recorded by optical inspection of the specimen's edge during a test. Progressive damage within the body of specimens was obtained by X-ray computed tomography (CT) scanning. Scanning Electron Microscope (SEM) images of the failed fracture surfaces provided a valuable insight into the fracture mechanisms from a microscopic perspective.

2 Specimen design and manufacture

A new specimen layup (as shown in Fig. 1), which was modified from the layup used in [26], was designed here in order to investigate delamination migration at a +θ/-θ centreline interface. The layup in the upper half of the original 0/θ stacking sequence, as highlighted in the box in Fig. 1a, was chosen to achieve an anti-symmetric stacking sequence. In the current layup, two blocks of 2 plies ($+\theta_2/-\theta_2$) were used to replace the original θ_4 ply block as mark in red in the Fig. 1b, which will allows two separate migration events. The fibre orientations, θ, studied were 60^o and 75^o.

Classical laminated plate theory was used to select a layup suitable for the test, with reduced thermal distortions during curing and minimised coupling effects at the delamination front during loading. In order to quantitively characterise the coupling effect, D_c was proposed by Davidson et al. [27], which indicates the curvature due to longitudinal/transverse bending coupling. And B_t was proposed by Sun and Zheng [28], which indicates the skewness of the crack profile due to bending/twisting coupling [12]. D_c and B_t depend on the bending stiffness matrix coefficients D_{ij} according to:

$$D_c = \frac{D_{12}^2}{D_{11}D_{22}}, B_t = \frac{|D_{16}|}{D_{11}}$$

For the full specimen (lower + upper sub-laminates) studied here, D_c was less than the proposed limit of 0.25 [29] and B_t = 0 for both fibre orientations tested. In addition, they do not exhibit bending/twisting, tensional/bending and shearing/twisting coupling because both upper and lower sub-laminates are balanced and anti-symmetric. There will be some bending/shearing coupling in the layup that could cause opposing in-plane shear forces in the laminates. Numerical results show that the resultant shear strain energy release rate at the initial crack front is negligible, which means the delamination is highly mode I dominated. The effect of shear coupling on the asymmetry of the damage initiation can thus be assumed to be very limited.

The material system used in this study was Hexcel's HexPly® IM7/8552 carbon/epoxy prepreg, with a 0.125 mm nominal ply thickness. The material properties for IM7/8552 are: E_{11} = 161.0 GPa, E_{22} = E_{33} = 11.38 GPa, G_{12} = G_{13} = 5.17GPa, G_{23} = 3.98GPa, v_{12} = v_{13} = 0.32, v_{23} = 0.436, G_{Ic} = 0.2N/mm, G_{IIc} =1.0N/mm [17]. One panel was manufactured using hand lay-up for each stacking sequence (θ equals to 75^o or 60^o), followed by curing in an autoclave (2 h at 180 °C with 100 psi pressure). The ''||'' symbol in Fig. 1 indicates the location of the 12 micron PTFE film. This insert

spans the specimen's width, b, and creates a starter delamination of length a_0. This insert thickness was chosen to satisfy that used in standard fracture toughness tests [8], and thus was considered to have negligible influence on the subsequent delamination behaviour. A wet diamond saw was used to cut the rectangular plates into individual DCB specimens with length l = 175mm, width b = 20mm and thickness h = 7mm, which are schematically shown in Fig. 2.

3 Experimental method and scheme

Prior to testing, the dimensions of individual specimen were measured and recorded. The edges of each specimen were covered with a thin layer of white paint to better visualise delamination growth and migration during the tests. A calibrated scale with a 1 mm increment was attached to each edge in order to help monitor delamination growth and locate migration position. As shown in Fig. 2, mechanical loading was introduced to the specimen through hinges bonded on each side. The specimen surfaces to be bonded were sanded and degreased, prior to bonding loading hinges with Araldite 2011.

All the tests were conducted using an Instron machine equipped with a 1 kN load cell. Measurements of load and cross-head displacement were recorded automatically using a data logger. Two test procedures were adopted for quasi-static tests: single-step and interrupted. In the single-step tests, specimens were loaded until either migration was observed on both lateral edges of the specimen, or a maximum delamination length of 40 mm from the PTFE insert front was reached. In the interrupted tests, loading of the specimens was stopped at significant points, such as load drops or delamination migration, previously observed during the single-step tests. All the quasi-static tests were conducted in displacement control, with a constant displacement rate of 0.5 mm/min. This slow rate allows a more effective observation of the crack propagation. The fatigue

tests were run at various percentages of the displacement at which initial delamination growth was seen to occur. The percentage of the quasi-static load is commonly referred to as ‘severity’ in the literature. Interrupted fatigue tests were only conducted for specific severities and were interrupted after various extents of stiffness loss, to observe the progressive damage process. All the fatigue tests were conducted under displacement control at constant amplitude, with an *R* ratio of 0.1 and a frequency of 5~6 Hz. For selected specimens, the near-tip regions were sectioned and inspected via destructive optical microscopy or SEM. In addition, specimens experiencing interrupted tests were inspected using non-destructive X-ray CT in order to gain an understanding of the fracture mechanisms within the body of the specimens. To improve X-ray contrast, the samples from interrupted tests were soaked in a bath of zinc iodide penetrant for 3 days. Micro X-ray CT scanning was conducted at the UK National Composites Centre (NCC), where a Nikon XTH225ST CT scanner was used. It has a 1 μm focal spot size and 225 kV, 225W micro-focus X-ray source. Each scanned sample was mounted on the rotation stage and positioned between the X-ray source and the 2000×2000 16 bit pixel panel detector. A voxel size of ~20μm is achieved. Post-processing on the scan results was performed using the VG Studio Max 2.1 and Avizo® 7 software packages.

Three specimens were chosen to conduct quasi-static tests in order to have a basic understanding of the whole damage process and another three specimens were used for the interrupted tests. For the specimens with $\theta=75^{o}$, fatigue tests were conducted at 62.5%, 68.75%, 75% and 100% of the delamination onset displacement. 68.75% of the delamination onset displacement was chosen for fatigue interrupted test and marked by ‘*’ in Table 1. With regard to the specimens with $\theta=60^{o}$, fatigue tests were carried out at 70%, 80%, 90% and 100% of the delamination onset displacement. 100% of the delamination onset displacement was chosen for fatigue interrupted test and also

marked by '*' in Table 1. The value of delamination onset displacement was determined by the point with 5% increase in compliance from the original linear region of the quasi-static load displacement curve. Table 1 shows details of the total number of specimens tested and the number of interrupted tests.

4 Experimental results

Quasi-static and fatigue test results for the two specimen types, containing centre 75^o/-75^o and 60^o/-60^o interfaces, are shown below separately. Pictures taken from both edges are presented to provide information on the progressive damage behaviour. Further details of delamination and migration mechanisms inside the specimens are presented and discussed in what follows.

4.1 Quasi-static and fatigue tests for specimens with $\theta = 75^o$

4.1.1 Quasi-static tests

A representative load versus cross-head displacement curve recorded during the single step tests for specimens with $\theta = 75^o$ is shown in Fig. 3. The response is approximately linear in stage I followed by a region of nonlinearity, which indicates the onset of damage. In stage II, the load slowly increased with displacement, due to small amount of crossover fibre bridging in the wake of the crack tip, which restrained crack opening. A significant load drop happened at the end of stage II, where an unstable event (i.e. migration) occurred quickly from the PTFE film. The latter stage III corresponds to the continued migration and propagation of the delamination. More ply splits and induced delamination occurred at the stages III and IV. The stiffness of specimens gradually decreased with increasing displacement throughout all stages. In order to better understand the progressive failure behaviour, three interrupted tests were conducted. As shown in Fig. 4, three specimens were loaded until obvious load drops, which correspond to the end of stages II, III and IV,

respectively.

After the interrupted specimens were removed from the test set-up, edge views at key stages were captured using an Olympus SZX16 microscope. The image scales of the different interrupted specimens may be different, but the front and rear views for each specimen are at the same scale. This applies to all the following edge views for the interrupted specimens studied here. As can be seen in Fig. 4, the delamination firstly propagated along the pre-cracked interface, i.e. the centre $+75^o/-75^o$ interface (see the notation of interfaces and ply blocks in Fig. 2 for better understanding). When the load reached a critical value, transverse matrix cracks (ply splits) developed in the adjacent lower -75^o ply block due to large tensile stress and weak transverse strength of the ply. Subsequently, the delamination migrated through the ply splits and propagated across the width of the specimen, following the -75^o fibre direction. A new delamination was then induced close to or just inside, the lower -75^o ply block at the lower $-75^o/+75^o$ interface and propagated backwards, in the direction against the main crack propagation direction. This delamination is a direct result of the ply splits developed in the lower -75^o ply block. With the delamination growing further, transverse ply splits also initiated in the lower $+75^o$ ply block for the same reason and delamination began to propagate in the lower $+75^o$ ply block, as shown from the exposed $+75^o$ fibres on a typical failed fracture surface after opening the tested specimen in Fig. 5. The ply splits that initiated in the lower $+75^o$ ply block finally induced another new delamination approaching the lower $+75^o/0^o$ interface. This second interface crack extended through the width along the $+75^o$ fibre direction and propagated forward. The whole above migration initiation was indicated by a very significant drop in load at the end of stage II. With further loading, more ply splits (visible on both edge views) developed and moderately stable delaminations approximately propagated along the initial centre

+75º/-75º, adjacent -75º/+75º and +75º/0º interfaces, at the same time. The second load drop at the end of stage III was mainly caused by the delamination along the lower +75º/0º interface. The subsequent load drops may be caused by the completion of the migration events and/pull-out of bridging fibres. Delaminations were finally connected by the ply splits and delamination growth continued along the lower +75º/0º interface without further migration.

The discussion given above was confirmed by X-ray CT scan results of the interrupted tests. Figs. 6 and 7 show X-ray CT scan results of two quasi-static specimens (with $\theta = 75^{o}$), which were respectively loaded and interrupted to the first large load drop (interrupted test 1) and the second load drop (interrupted test 2). All damage that can be observed in the CT scanned specimens is shown in these figures. All the 2D views were taken looking in the specimen thickness direction (Z-axis), as marked in Fig. 2. The grey in some images is used as background to enhance contrast, which is also helpful for locating the position of damage in the width direction. This applies to all the following CT scan images. Each image in the table shows the damage status in the specific ply blocks, along with an image of the overall damage in the specimen. The damage that happened in the specimen is mostly in the form of delaminations along the centre +75º/-75º, adjacent lower -75º/+75º and +75º /0º interfaces, with extensive ply splits in the lower -75º ply block and +75º ply block of lower arm, which are distributed through the entire width of the specimen and along the length direction. When the applied load reached the maximum value, various damage events occurred nearly simultaneously. Although the delamination migrated downwards from the insert film front into the lower arm, there is a certain amount of splitting in the adjacent upper +75º ply block of the upper arm.

As shown in Fig. 7, with further loading until the second load drop in interrupted test 2, the

number of splits in the lower +75^{o} ply block increased obviously. In addition, delaminations along the centre +75^{o}/-75^{o}, adjacent lower -75^{o}/+75^{o} and +75^{o}/0^{o} interfaces grew at the same time. While delamination on the lower +75^{o}/0^{o} interface was mainly responsible for the second load drop in the load versus displacement curve.

4.1.2 Fatigue tests

The value of displacement corresponding to the point with 5% increase in compliance from the original linear region of the quasi-static load displacement curve is 2.0 mm. Three specimens were tested at 68.75% severity and a single specimen tested at 62.5%, 75% and 100% severities. Fig. 8 shows the fatigue stiffness losses for all the cases as the number of cycles increases. The peak load is normalised by its value for the first cycle. For the majority of the specimens, once damage started to propagate there was an initial decrease in the stiffness, and the peak load continually decreased with delamination damage development. While for the specimen tested at 62.5% severity, the normalized maximum load curve then leveled out at approximately 85% of the normalized maximum load. This can be explained as the driving force not being large enough to complete the delamination migration from the initial mid-plane to the adjacent -75^{o}/75^{o} interface.

At the same 68.75% severity, fatigue loading applied to the three specimens was terminated when they had 20%, 25% and 30% stiffness losses, respectively. The post-mortem edge views of the samples are shown in Fig. 8. The damage sequences under fatigue loading are similar to the quasi-static scenario. Transverse splits firstly occurred in the upper +75^{o} ply block (upper arm) and lower -75^{o} ply block (lower arm) adjacent to the mid-planar interface. Then ply splits in the lower -75^{o} ply block induced delamination along the lower -75^{o}/+75^{o} interface. Meanwhile, splits initiated in the lower +75^{o} ply block and induced delamination along the lower +75^{o}/0^{o} interface.

4.2 Quasi-static and fatigue tests for specimens with $\theta = 60^o$

4.2.1 Quasi-static tests

A representative load versus cross-head displacement curve recorded during the single step tests for specimens with $\theta = 60^o$ is shown in Fig. 9. The load-displacement curves of the three interrupted tests are presented in Fig. 10. Similar to the 75^o case, the response is linear in stage I. Then, the specimen stiffness decreased gradually with transverse ply splits occurring around the PTFE film, which can be seen from the front view image of interrupted test 1, as illustrated in Fig. 10. While at the rear side, the delamination almost grew along the pre-cracked plane. At the end of stage II, the load exhibited a small drop. From both side views of the interrupted test 2, it can be seen that delamination had already migrated from the pre-cracked plane through the adjacent lower -60^o ply block and propagated across the width of the specimen following the -60^o fibre direction, towards the rear edge of the specimen (as shown in Fig. 11b for a typical fracture surface of tested specimens). A new delamination induced on the adjacent lower $-60^o/+60^o$ interface and propagated forwards. At stage III, the load slowly increased with displacement. Additionally, more transverse splits occured during this period. The load drop at the end of stage III may mean the completion of first migration or the pull-out/breaking of bridging fibres. The stage IV corresponds to the continued propagation of the delamination along the lower $-60^o/+60^o$ interface and the second delamination migration, which causes the delamination to a transition toward the lower $+60^o/0^o$ interface and the obvious load drop at the end of stage IV, in the same manner as the first migration event. The two complete migration events can be seen from the front and rear views in Fig. 11a.

Figs. 12 and 13 show X-ray CT scans of two quasi-static specimens (with $\theta = 60^o$). One specimen was loaded to the stage IV and then interrupted (interrupted test 3), and the other specimen was

tested to full failure in a single step. Compared with the specimens of $\theta = 75^o$, the specimens with $\theta = 60^o$ exhibited the same damage types, including mainly ply splits and delamination. However, there were no matrix splits in the adjacent upper $+60^o$ ply block of the upper arm. Furthermore, the delaminated area created during the first migration process was larger in the $\theta = 60°$ coupons, which exhibited a more gradual stiffness degradation after the damage onset. It seems that extensive ply splitting in the lower $+60^o$ and -60^o ply block acted to dissipate energy more gradually and the tortuosity of the crack path prevented dramatic stiffness loss. When the specimen was loaded to the point beyond stage IV, both delamination and splits were extended, as shown in Fig. 13. The load drop at the end of stage IV indicates the end of the migration process. Increasing loading resulted in stable growth of delamination along the lower $+60^o/0^o$ interface, which grew uniformly in the width direction.

4.2.2 Fatigue tests

The average value of displacement corresponding to the initiation point is 1.65 mm. Three specimens were tested at 100% severity and a single specimen at 70%, 80% and 90% severity. Fig. 14 shows the fatigue stiffness losses for all the cases. Unlike the non-monotonic variation trend in the specimens with $\theta=75^o$ at very low severity, the normalized maximum load gradually decreased with the number of applied cycles. This means that the fatigue delamination process is relatively more progressive in the specimen with $\theta=60^o$. This behaviour also occured in the quasi-static tests, since there was no suddenly large load drop when initial damage occurred.

At 100% severity, fatigue loading on the three specimens was terminated when they had 22%, 24% and 25% stiffness losses, respectively. The edge views taken when the tests were paused are also shown in Fig. 14. The damage sequence under fatigue loading is similar to the quasi-static case.

Delamination on the pre-cracked plane started to migrate from several locations near the insert tip and grew along the -60^o fibre direction towards front and rear edges. The new induced delamination then propagated along the lower -60^o/+60^o interface. Fig. 15 shows a typical fracture surface of a tested specimen. Both in the quasi-static and fatigue test, the migrated areas during the migration event are larger than the specimens with θ=75^o. The energy dissipation process is relatively stable and slow.

In order to trace the second migration event, the three specimens after interrupted tests were fatigue tested again with a higher displacement loading until their crack tips reached a same location, which is close to the second migration point. They were then applied with same value of loading displacement and stopped after different numbers of cycles in order to record the edge views before and after the second migration, which are shown in Fig. 15. The delamination firstly grew along the lower -60^o/+60^o interface. The clear trend to migrate into the lower +60^o ply block can be seen from a series of ply splits, as shown in the front view. With more ply splits developed, delamination subsequently migrated into the neighbouring lower +60^o/0^o ply interface. At this interface the driving force was parallel to the 0^o ply orientation, and the condition for rapid delamination growth was met. Hence, there was rapid and smooth delamination growth within this ply interface.

5 Fracture surface analysis

The delamination propagation mechanisms described above are graphically illustrated in Figs. 16a and b. These figures schematically show the shape of crack propagation in the thickness of a specimen. The delaminated area includes three different areas: the pre-cracked area, the triangular-shaped crack area and the interply crack area. When delamination initiated at the end of

the pre-cracked area, the delamination path migrated into the lower $-\theta_2$ ply block from the specimen pre-cracked plane. A triangular-shaped area, which can be observed very clearly with the naked eyes, was then formed. This triangular-shaped area was not strictly at the centre $+\theta/-\theta$ interface but rather slightly inside the lower $-\theta_2$ ply block. Similarly, the delamination path deviated from the $-\theta/+\theta$ interface and migrated into the lower $+\theta_2$ ply block to form another triangular-shaped area. Part of the triangle area formed inside the lower $-\theta_2$ ply block and others inside the lower $+\theta_2$ ply block since both $-\theta$ and $+\theta$ fibres were exposed. After passing by the triangular-shaped areas, the delamination propagated near the $+\theta/0$ interface. Figs. 16c and d present the 3D sketches of the fracture surfaces for specimens with $\theta = 75^o$ and 60^o. The fracture surfaces between quasi-static test and fatigue tests are similar for both kinds of specimen. Transverse ply splits existing in the lower $+\theta_2$ ply block can be observed from the front edge of tested specimens. The triangular shapes varied with respect to the value of θ and the triangular-shaped area became larger as the fibre angle θ increased, as illustrated in Figs. 16c and d. X_1 and X_2 are the horizontal distances of the point of first migration to the front of PTEF insert, along the length direction, which are introduced to quantitatively analyse the fracture surfaces. The detailed values, average values and standard deviations of X_1 and X_2, are listed in Table. 2. Fig. 17 gives the comparison of the values of X_1 and X_2 between quasi-static and fatigue specimens. It shows that the average values of X_1 and X_2 for quasi-static specimens are slightly higher than under fatigue loading.

After exposing the specimen fracture surfaces, details of the migration became apparent and fractographic analysis was implemented for more in-depth understanding on the detailed failure mechanism and root cause of failure. All the SEM micrographs reported in the subsequent images correspond to the fracture surface of lower arm unless otherwise noted. Fig. 18 brings together the

micrographs at specific locations on the fracture surface from a specimen ($\theta = 75^o$) under quasi-static loading. Either exposed fibres or imprints are observed on the fracture surfaces, which illustrates that delamination does not usually grow cohesively through the interply resin-rich region, but interfacially adjacent to one ply of an interface [30]. Figs. 18b and c show SEM images of the upper fracture surface in the area close to the PTFE insert front. The surface is matrix dominated, which shows imprints of the 75^o fibres. The delamination along the mid-plane transitioned into the lower -75^o ply block, immediately after onset from the PTFE film insert front. The slightly inclined cusps in Fig. 18e, which are caused by the extensive yielding (ductility) of the matrix [31], indicate the presence of local shearing at the delamination front. The orientation of the fibre imprint, along with evidence from the X-ray CT scanning results, suggests that delamination propagates along the -75^o fibre direction towards the edges of the specimen. The intralaminar delamination that propagated in the lower -75^o ply block gradually kinked into the lower $+75^o$ ply block, as indicted by the 75^o fibres visible in the Figs. 18d, f and g. Especially at the transition area as shown in Figs. 18d and f, the rough fracture surface means more energy dissipation during this transition process, accompanied with obvious broken fibres and matrix debris. Broken fibres are typical of the occurrence of fibre bridging [32] and the presence of broken fibres and matrix debris here may be caused by the breaking of bridging fibres when the specimens were broken open. As the delamination grew further, the stress state favored kinking through the lower $+75^o$ ply block, leading to eventual migration. The lower zero degree ply prevented further kinking since it was energetically unfavorable, the obvious zero degree fibres in Fig. 18i also indicated that the delamination tended to kink into the lower zero degree ply but was finally prevented from doing so, hence delamination proceeded near the lower $+75^o/0^o$ interface along the 0^o fibre direction, as

shown in the Fig. 18h. SEM images of a fatigue specimen containing a +75°/-75° interface are shown in Fig. 19. Compared with the quasi-static specimen, the appearance of fatigue fracture surface of the fatigue specimen is smoother with fewer damage features presented [33]. It may mean that less energy is dissipated in the fatigue induced delamination, since the energy release by a crack extension is related to the roughness and damage features appearing on the fracture surface [33]. The delamination grew along the -75° fibre direction from the insert front and the tendency to migrate through the lower -75° ply block was obvious, which could be judged from the orientations of cusps and clear ply splits as shown in Figs. 19b and c. The regions in Figs. 19d and e contain clean looking -75° fibre imprints with shear cusps nested between the fibres. This indicates a mixed mode I/II form of loading along this -75°/+75° interface. Fig. 19f shows the transition of the propagating delamination from interfacially adjacent to the lower -75° ply to interfacially adjacent to the lower +75° ply. The matrix dominated morphology presented initially, gradually changes to fibre interface dominated as shown in Fig. 19g. Figs. 19h and i show the delamination surface close to the lower +75°/0° interface, which contained river lines that are indicative of mode I dominated fracture [24].

Fig. 20 shows the SEM images of the fracture surface from one quasi-static specimen with θ=60°. The delamination initiated gradually from the mid-plane and propagated along the -60° fibre direction and towards the rear side of the specimen (similar to what was discussed before for the θ=75° case). Exposed -60° fibres, broken fibres, matrix debris and ply splits can be observed in Figs. 20b and c. The developed ply splits promote the delamination to migrate towards the lower interface. At one instance, there was sufficient crack driving force to migrate delamination into the lower -60°/+60° interface and initiate delamination along this new propagating interface. After the

first migration event, the delamination presented two different features as shown in the SEM images (Figs. 20d, e and g); the area near the rear side of the specimen, exhibiting lines aligned to the -60^o fibre direction, and the area near the front side, characterised by oblique lines, aligned to the +60^o fibre direction. The first feature means that the migrated delamination turned back to the original mid-plane. While most of the triangle area presented intralaminar cracking in the lower +60^o ply block. This observation may be caused by a high variation in driving force across the width of the specimen. The delamination finally migrates through the lower +60^o ply block, as shown in Fig. 20f, until it reaches the lower +60^o/0^o interface, at which the zero degree ply is approximately parallel to the driving force. Fibre imprints and broken fibres were the main feature in Fig. 20h, whereby the river lines indicated the delamination along the lower +60^o/0^o interface is mode-I dominated fracture.

The main features of fatigue fracture surfaces are similar with the quasi-static ones. Less fibre bridging was observed on both edges of the fatigue specimens. Compared with the quasi-static case, relatively cleaner surfaces of fatigue specimen and fewer broken fibres were observed in Fig. 21, which was consistent with the results reported in Ref. [33] and may be caused by the wear away of asperities under fatigue loading. In addition, under displacement control, load is reduced in fatigue tests once damage has initiated, while this is not the case for the quasi-static case where displacement increases monotonically. This may also give an additional explanation to the difference between fatigue and quasi-static fracture surfaces.

6 Discussion and conclusions

Using the simple DCB set-up, quasi-static and fatigue delamination migration tests were conducted for specimens with centre +75^o/-75^o and +60^o/-60^o ply interfaces. All the specimens for

both quasi-static and fatigue loading had a fairly similar sequence of damage events and migration mechanisms, with ply splits developing inside the specimens and finally resulting in delamination migration. The presence of these ply splits promotes the delamination to migrate such that the induced delamination finds an ideal path with the lowest fracture resistance. The formation of ply splits is likely to be due to the magnitude of the matrix stress being close to the matrix strength.

The fractographic results show that fibre imprints, shear cusps and broken fibres are the main surface damage features for both quasi-static and fatigue fracture surfaces. In Ref. [34], it indicated that the most significant differences in morphology correspond to striations and rollers, which are often highly localised and can be difficult to find here. One interesting comparison between the quasi-static and fatigue fracture surfaces is that the fracture surface after quasi-static loading is rougher, with more cusps, than the fatigue case. The formation of the cusps leads to an overall increase in fracture energy absorption [30]. Hence, it indicates that more energy was dissipated in the quasi-static specimen for the same fracture area. Another interesting comparison is that the distances (i.e. X_1 and X_2) from migration points to the pre-crack tip are slightly smaller in the specimens under fatigue loading. One possible reason behind this difference is that more ply splits were formed in the fatigue specimens, which promotes the earlier migration of delamination. From the viewpoint of released energy, less energy was taken on the formation of shear cusps or fibre bridging, while more energy was dissipated on the development of ply splits for the specimens under fatigue loading. The validity of this explanation still needs further investigation.

The behaviour of the delamination after initiation will depend on the orientation of the ply adjacent to the delamination propagation. Delamination growth exhibits inherent directionality, which preferably grows parallel to either the lowermost or the uppermost fibre direction at a ply

interface, depending upon the sign of the shear stress [30]. At the second triangular area of the studied specimens, intralaminar cracks in both the θ and –θ plies can be observed, which means a high variation in driving force across the width of the specimen at this area. The stacking sequence has an influence on the triangular area and a smaller value of θ exhibits a larger triangular area. For the specimens with $\theta = 60^o$, there is a gentle and steady delamination growth process after the first migration event, as seen from the larger triangular area. Specimens still have load bearing and fracture resistance capacity (seen from the load vs. displacement curve in Fig. 9 and the area under this curve) after delamination initiation. This could provide an opportunity for early warning of damage during in-service loading, unlike the unconstrained and self-similar delamination growth in unidirectional laminates. It might be feasible to promote delamination migration (increase the tortuosity of the crack path) and thus enhance damage tolerance of composite structures by careful tailoring of the stacking sequence.

In this study, the delamination always ends up along a θ/0 interface whether the specimens are subject to quasi-static or fatigue loading. Since the off-axis plies are prone to ply splits, this allows the inherent migration event for delamination between multidirectional ply interfaces until delamination reaches the 0^o ply that prevents further migration. Therefore, it is necessary to include the migration process in delamination simulation in multidirectional laminates. Since the test results exhibit a high level of reproducibility, they could be used to validate numerical models for capturing delamination migration and intralaminar fracture. The results presented in this paper are based on controlled laboratory specimens and not real aircraft components. The knowledge acquired through this work can be extended to other fibre angle interfaces or other loading scenarios where migration is known to occur in a similar manner. Furthermore, better understanding and

simulation of delamination propagation and migration at multidirectional ply interfaces can be exploited in damage tolerant design. Future work is required to investigate the effects of asymmetry of the crack front and width of specimens on the migration mechanisms.

Acknowledgement

The authors acknowledge the help and guidance of Mike I. Jones and Supratik Mukhopadhyay for producing the CFRP laminates and O. J. Nixon-Pearson for carrying out the CT scanning. Yu Gong would like to gratefully acknowledge financial support from the China Scholarship Council and the Academic Excellence Foundation of BUAA for PhD Students.

References

[1] Zhao L, Wang Y, Zhang J, Gong Y, Hu N, and Li N, XFEM-based model for simulating zigzag delamination growth in laminated composites under mode I loading. Compos Struct, 2017; 160: 1155-1162.
[2] Zhao L, Wang Y, Zhang J, Gong Y, Lu Z, Hu N, and Xu J, An interface-dependent model of plateau fracture toughness in multidirectional CFRP laminates under mode I loading. Compos B Eng, 2017; 131: 196-208.
[3] Gong Y, Zhao L, Zhang J, and Hu N, An improved power law criterion for the delamination propagation with the effect of large-scale fiber bridging in composite multidirectional laminates. Compos Struct, 2018; 184: 961-968.
[4] Ning H, Li J, Hu N, Yan C, Liu Y, Wu L, Liu F, and Zhang J, Interlaminar mechanical properties of carbon fiber reinforced plastic laminates modified with graphene oxide interleaf. Carbon, 2015; 91: 224-233.
[5] Chen Y, Wang S, Liu B, and Zhang J, Effects of geometrical and mechanical properties of fiber and matrix on composite fracture toughness. Compos Struct, 2015; 122: 496-506.
[6] Chen BY, Tay TE, Pinho ST, and Tan VBC, Modelling delamination migration in angle-ply laminates. Compos Sci Technol, 2017; 142: 145-155.
[7] Canturri C, Greenhalgh ES and Pinho ST, The relationship between mixed-mode II/III delamination and delamination migration in composite laminates. Compos Sci Technol, 2014; 105: 102-109.
[8] ASTM. Standard Test Method for Mode I Interlaminar Fracture Toughness of Unidirectional Fiber-Reinforced Polymer Matrix Composites. ASTM International, West Conshohocken PA, 2007, DOI: 10.1520/D5528_D5528M.
[9] ASTM, Standard test method for mixed mode I-mode II interlaminar fracture toughness of uniderectional fiber reinforced polymer matrix composites, ASTM D6671/D6671M-06; 2006.
[10] Robinson P and Song DQ, A modified DCB specimen for mode I testing of multidirectional laminates. J Compos Mater, 1992; 26(11): 1554-1577.
[11] Sebaey TA, Blanco N, Costa J, and Lopes CS, Characterization of crack propagation in mode I

delamination of multidirectional CFRP laminates. Compos Sci Technol, 2012; 72(11): 1251-1256.
[12] Prombut P, Michel L, Lachaud F, and Barrau J, Delamination of multidirectional composite laminates at 0°/θ° ply interfaces. Eng Fract Mech, 2006; 73(16): 2427-2442.
[13] Hull D and Shi YB, Damage mechanism characterization in composite damage tolerance investigations. Compos Struct, 1993; 23(2): 99-120.
[14] Krueger R, Cvitkovich MK, O'Brien TK, and Minguet PJ, Testing and analysis of composite skin/stringer debonding under multi-axial loading. J Compos Mater, 2000; 34(15): 1263-1300.
[15] Greenhalgh E and Singh S. Investigation of the failure mechanisms for delamination growth from embedded defects. Proceedings of the 12th International Conference on Composite Materials, Paris (France), 1999.
[16] Canturri C, Greenhalgh ES, Pinho ST, Nilsson S, and AB SS, Delamination growth mechanism from embedded defects in compression. Proceedings of ICCM18, Jeju Island, 2011.
[17] Hallett SR, Green BG, Jiang WG, and Wisnom MR, An experimental and numerical investigation into the damage mechanisms in notched composites. Compos A Appl Sci Manuf, 2009; 40(5): 613-624.
[18] Peng L, Zhang J, Zhao L, Bao R, Yang H, and Fei B, Mode I delamination growth of multidirectional composite laminates under fatigue loading. J Compos Mater, 2011; 45(10): 1077-1090.
[19] Tao J and Sun CT, Influence of ply orientation on delamination in composite laminates. J Compos Mater, 1998; 32(21): 1933-1947.
[20] Zhao L, Gong Y, Zhang J, Wang Y, Lu Z, Peng L, and Hu N, A novel interpretation of fatigue delamination growth behavior in CFRP multidirectional laminates. Compos Sci Technol, 2016; 133: 79-88.
[21] Gong Y, Zhao L, Zhang J, Wang Y, and Hu N, Delamination propagation criterion including the effect of fiber bridging for mixed-mode I/II delamination in CFRP multidirectional laminates. Compos Sci Technol, 2017; 151: 302-309.
[22] Zhang J, Peng L, Zhao L, and Fei B, Fatigue delamination growth rates and thresholds of composite laminates under mixed mode loading. Int J Fatigue, 2012; 40: 7-15.
[23] Peng L, Xu J, Zhang J, and Zhao L, Mixed mode delamination growth of multidirectional composite laminates under fatigue loading. Eng Fract Mech, 2012; 96: 676-686.
[24] Ratcliffe JG, Czabaj MW and O'Brien TK, A Test for Characterizing Delamination Migration in Carbon/Epoxy Tape Laminates. NASA/TM-2013-218028, 2013.
[25] Ratcliffe JG and DeCarvalho NV, Investigating delamination migration in composite tape laminates. NASA/TM-2014-218289, 2014.
[26] Pernice MF, De Carvalho NV, Ratcliffe JG, and Hallett SR, Experimental study on delamination migration in composite laminates. Compos A Appl Sci Manuf, 2015; 73: 20-34.
[27] Davidson BD, Krüger R and König M, Three-dimensional analysis of center-delaminated unidirectional and multidirectional single-leg bending specimens. Compos Sci Technol, 1995; 54(4): 385-394.
[28] Sun CT and Zheng S, Delamination characteristics of double-cantilever beam and end-notched flexure composite specimens. Compos Sci Technol, 1996; 56(4): 451-459.
[29] Davidson BD, Kruger R and König M, Three dimensional analysis and resulting design recommendations for unidirectional and multidirectional end-notched flexure tests. J Compos Mater, 1995; 29(16): 2108-2133.

[30] Greenhalgh ES, Rogers C and Robinson P, Fractographic observations on delamination growth and the subsequent migration through the laminate. Compos Sci Technol, 2009; 69(14): 2345-2351.
[31] Naghipour P, Bartsch M, Chernova L, Hausmann J, and Voggenreiter H, Effect of fiber angle orientation and stacking sequence on mixed mode fracture toughness of carbon fiber reinforced plastics: Numerical and experimental investigations. Mater Sci Eng: A, 2010; 527(3): 509-517.
[32] Choi NS, Kinloch AJ and Williams JG, Delamination fracture of multidirectional carbon-fiber/epoxy composites under mode I, mode II and mixed-mode I/II loading. J Compos Mater, 1999; 33(1): 73-100.
[33] Amaral L, Yao L, Alderliesten R, and Benedictus R, The relation between the strain energy release in fatigue and quasi-static crack growth. Eng Fract Mech, 2015; 145: 86-97.
[34] Jollivet T and Greenhalgh E, Fractography, a Powerful Tool for Identifying and Understanding Fatigue in Composite Materials. Procedia Engineering, 2015; 133: 171-178.

Figure Captions

Fig. 1. Comparison between (a) the original 0/θ stacking sequence used in [26] and (b) the new +θ/-θ stacking sequence studied in the current work.

Fig. 2. Dimensions and test set-up of DCB specimen (unit: mm).

Fig. 3. Typical load vs. displacement curve of the tested specimens with $\theta = 75^o$.

Fig. 4. (a) Load vs. displacement curves of the interrupted tests for specimens with $\theta = 75^o$ and (b) edge views at key stages during the test, of the front side of the specimen ('Front view') and the rear side of the specimen ('Rear view'), the arrow marks the location of the initial crack tip and the scale visible is in mm.

Fig. 5. Quasi-static fracture surface for the tested specimens with $\theta = 75^o$.

Fig. 6. CT scan of a quasi-static specimen for the interrupted test 1.

Fig. 7. CT scan of a quasi-static specimen for the interrupted test 2.

Fig. 8. (a) Initial results obtained from the fatigue tests with $\theta = 75^o$ and (b) edge views at different stiffness losses during fatigue tests (the arrow marks the location of the initial crack tip and the scale visible is in mm).

Fig. 9. Typical load vs. displacement curve of the tested specimens with $\theta=60^o$.

Fig. 10. (a) Load vs. displacement curves obtained from the interrupted test for specimens with $\theta=60^o$ and (b) edge views at key stages during the tests (the arrow marks the location of the initial crack tip and the scale visible is in mm).

Fig. 11. (a) Front and rear views after the second migration event occurred and (b) Experimental fracture surface for the quasi-static specimens with $\theta = 60^o$.

Fig. 12. CT scan of a $\theta=60^o$ specimen tested quasi-statically and interrupted at stage IV (interrupted test 3)

Fig. 13. CT scan of a $\theta=60^o$ specimen tested quasi-statically to full failure.

Fig. 14. (a) Initial results obtained for the fatigue tests with 60^o/-60^o interface and (b) edge views at different stiffness losses during the first migration event (the arrow marks the location of the initial crack tip and the scale

visible is in mm).

Fig. 15. Experimental fracture surface for the fatigue specimens with $\theta = 60^o$ and edge views at different stiffness losses during the second migration event (the arrow marks the location of the initial crack tip and the scale visible is in mm).

Fig. 16. Delamination shape and path: (a) top view and (b) front view; 3D sketch of fracture surface for specimen (quasi-static and fatigue) with (c) $\theta = 75^o$ and (d) $\theta = 60^o$.

Fig. 17. Comparison of the value of X_1 and X_2 between quasi-static and fatigue specimens.

Fig. 18. Micrographs at different locations on the fracture surface from a quasi-static specimen ($\theta = 75^o$).

Fig. 19. Micrographs at different locations on the fracture surface from a fatigue specimen ($\theta = 75^o$).

Fig. 20. Micrographs at different locations on the fracture surface from a quasi-static specimen ($\theta = 60^o$).

Fig. 21. Micrographs at different locations on the fracture surface from a fatigue specimen ($\theta = 60^o$).

(a) Original 0/θ [22] layup

$[\theta/0/\theta_3/-\theta_4/-\alpha/-\theta/-\alpha/90/-\alpha/\alpha/90/\alpha/\theta/\alpha/\theta_4/-\theta_4/0//\theta_4/0/-\theta_4/-\alpha/-\theta/-\alpha/90/-\alpha/\alpha/90/\alpha/\theta/\alpha/\theta_4/0/-\theta_4]$

(b) Current 0/θ layup

$[+\theta_2/-\theta_2/0/-\theta_4/-\alpha/-\theta/-\alpha/90/-\alpha/\alpha/90/\alpha/\theta/\alpha/\theta_4/0/+\theta_2/-\theta_2//+\theta_2/-\theta_2/0/-\theta_4/-\alpha/-\theta/-\alpha/90/-\alpha/\alpha/90/\alpha/\theta/\alpha/\theta_4/0/+\theta_2/-\theta_2]$

Layup from left to right corresponds to the lower to the upper surface of the specimen.
'//' denotes location of PTFE film insert. θ = {60°, 75°}, α = 90°-θ

Fig. 1. Comparison between (a) the original 0/θ stacking sequence used in [26] and (b) the new +θ/-θ stacking sequence studied in the current work.

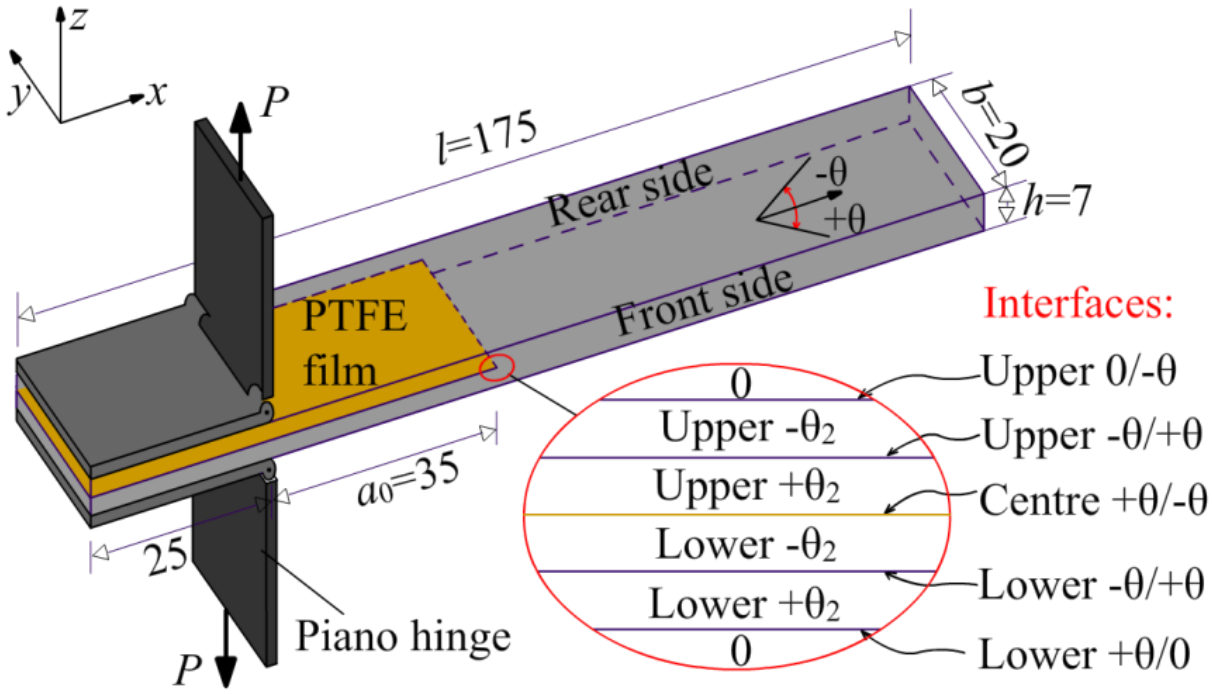

Fig. 2. Dimensions and test set-up of DCB specimen (unit: mm).

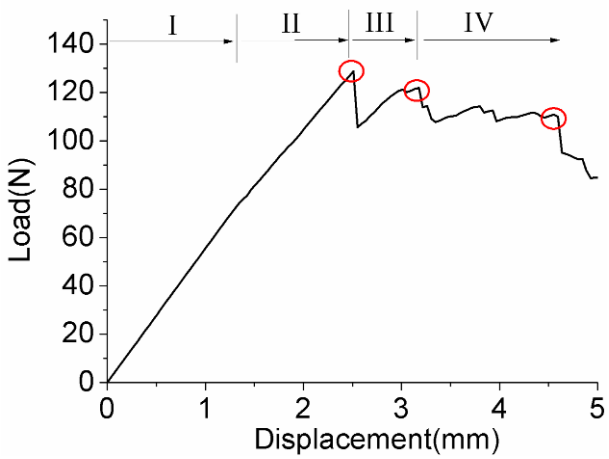

Fig. 3. Typical load vs. displacement curve of the tested specimens with θ = 75º.

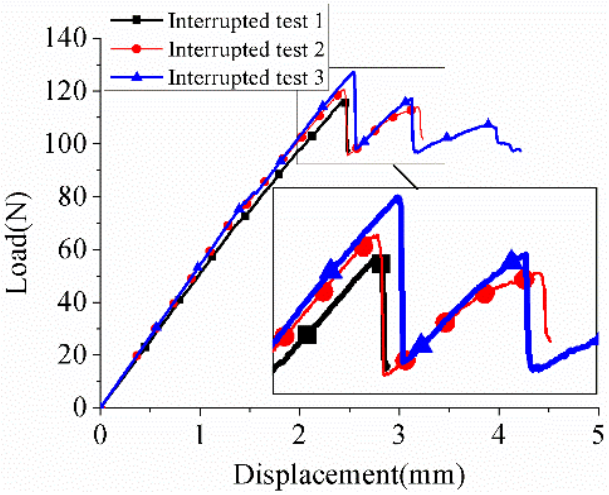

(a)

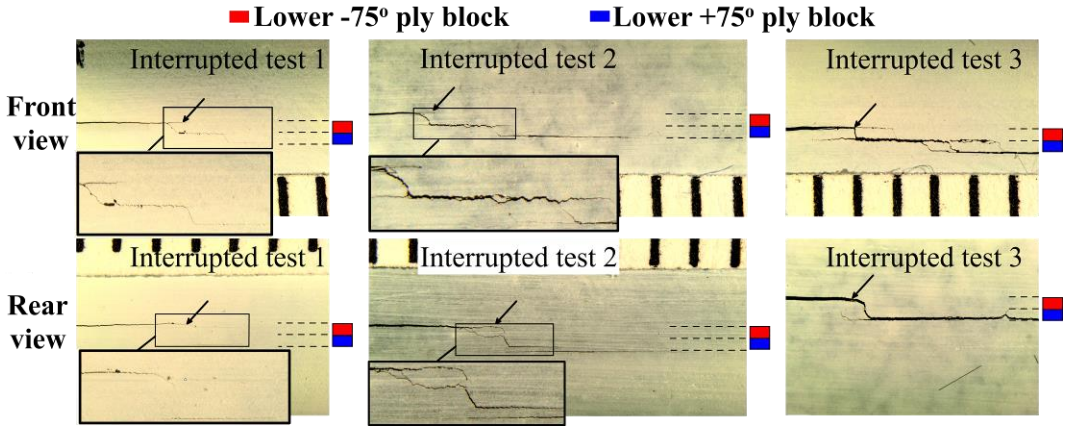

(b)

Fig. 4. (a) Load vs. displacement curves of the interrupted tests for specimens with θ = 75º and (b) edge views at key stages during the test, of the front side of the specimen ('Front view') and the rear side of the specimen ('Rear view'), the arrow marks the location of the initial crack tip and the scale visible is in mm.

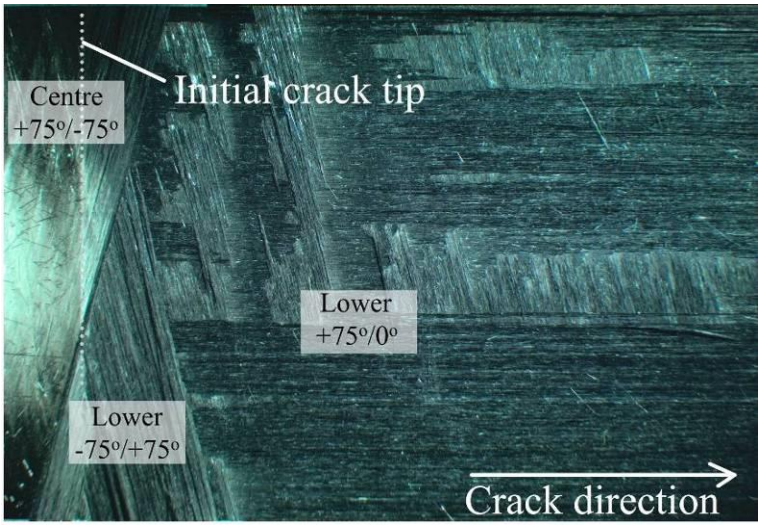

Fig. 5. Quasi-static fracture surface for the tested specimens with θ = 75º.

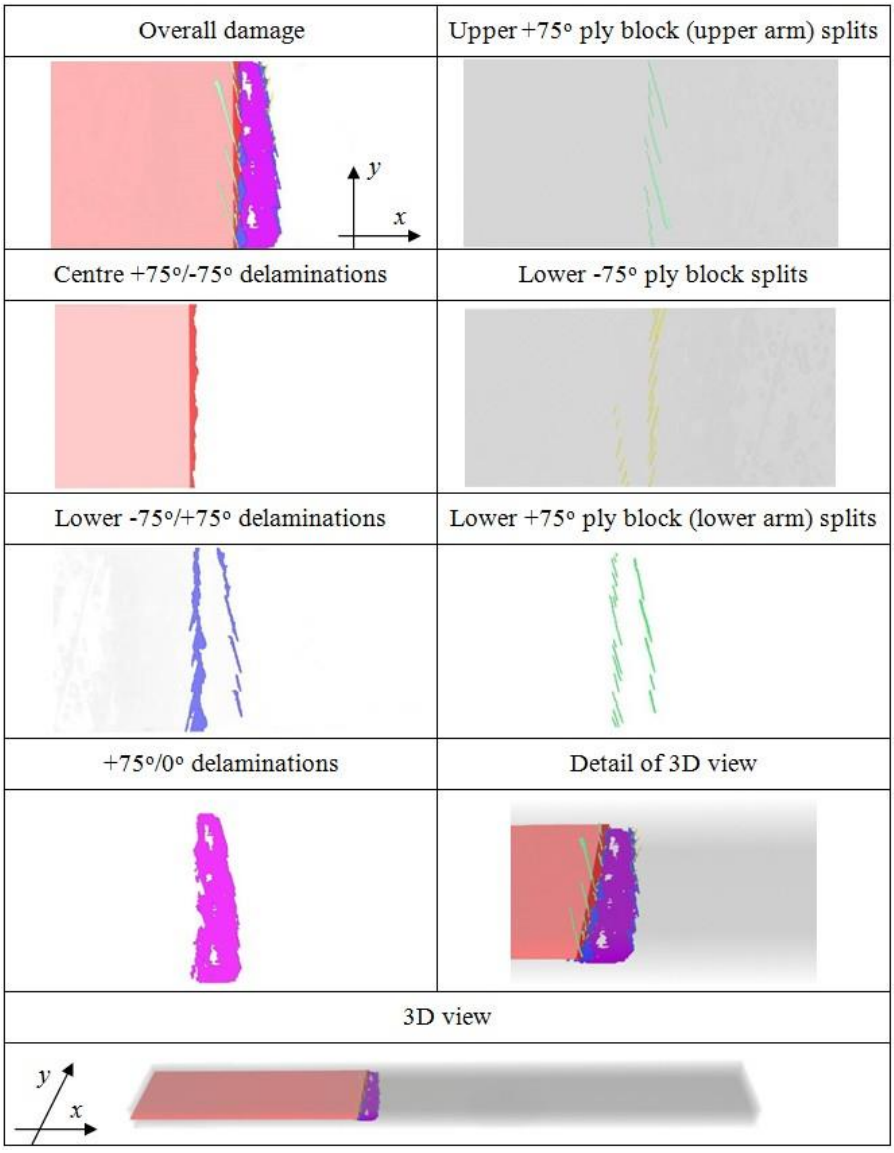

Fig. 6. CT scan of a quasi-static specimen for the interrupted test 1.

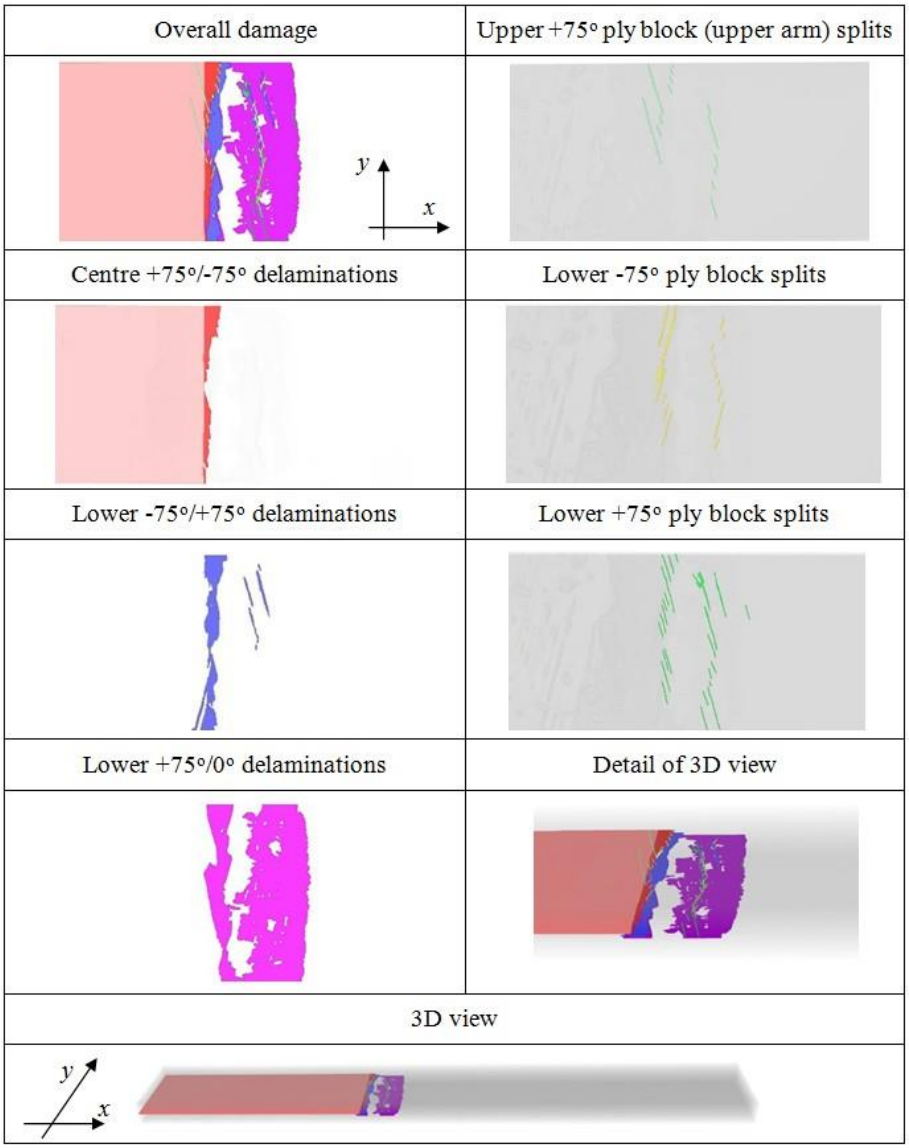

Fig. 7. CT scan of a quasi-static specimen for the interrupted test 2.

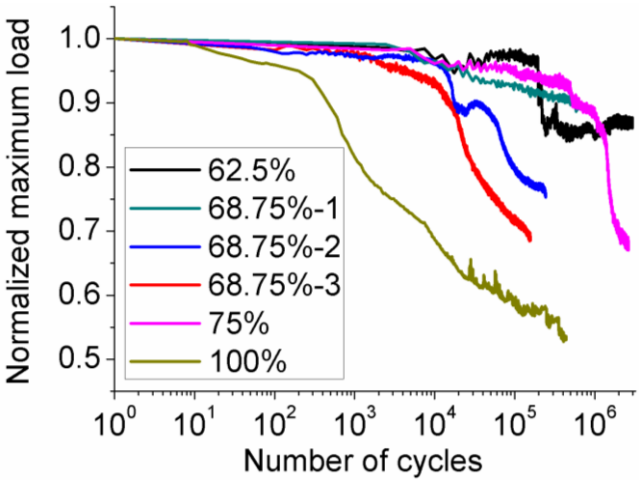

(a)

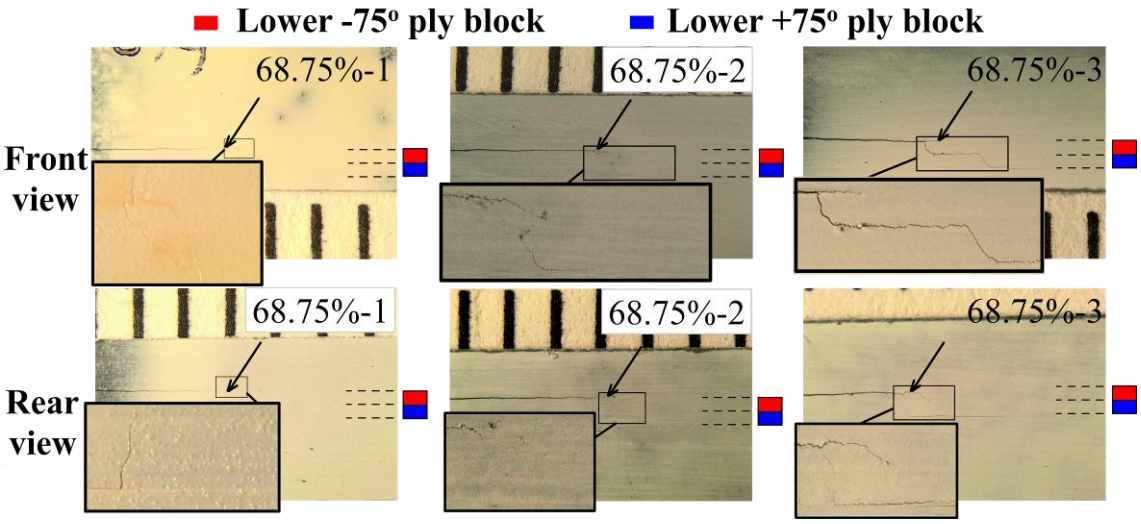

(b)

Fig. 8. (a) Initial results obtained from the fatigue tests with θ = 75º and (b) edge views at different stiffness losses during fatigue tests (the arrow marks the location of the initial crack tip and the scale visible is in mm).

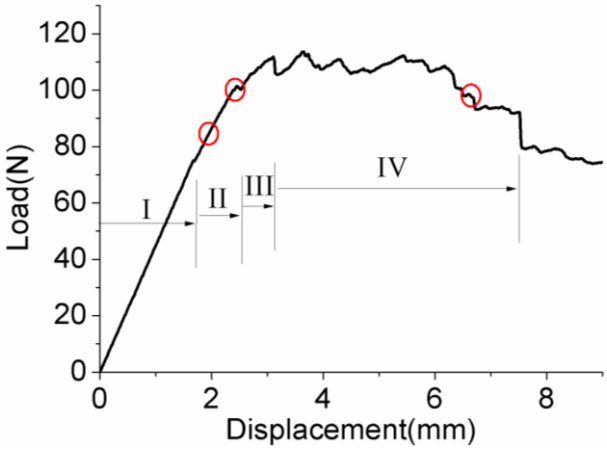

Fig. 9. Typical load vs. displacement curve of the tested specimens with θ=60º.

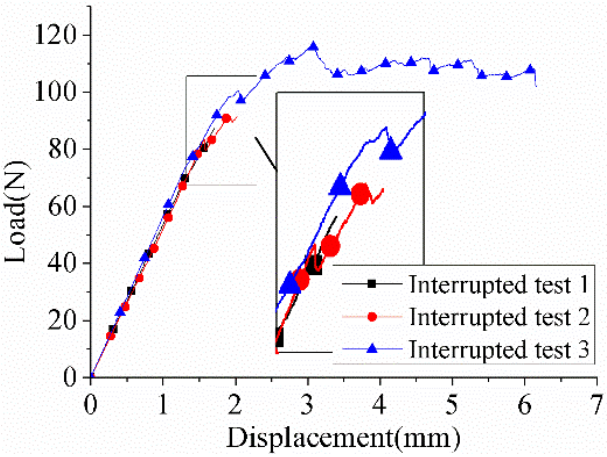

(a)

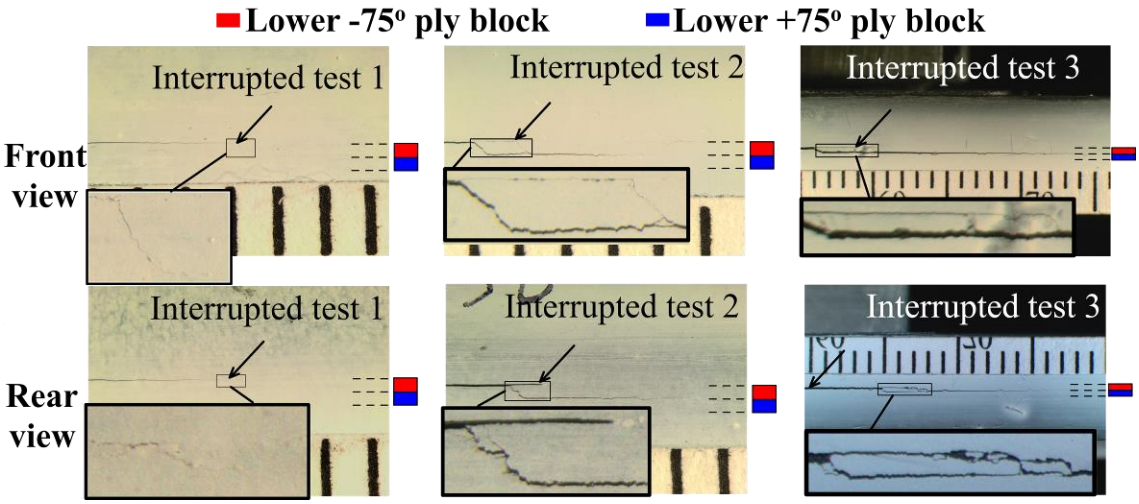

(b)

Fig. 10. (a) Load vs. displacement curves obtained from the interrupted test for specimens with θ=60º and (b) edge views at key stages during the tests (the arrow marks the location of the initial crack tip and the scale visible is in mm).

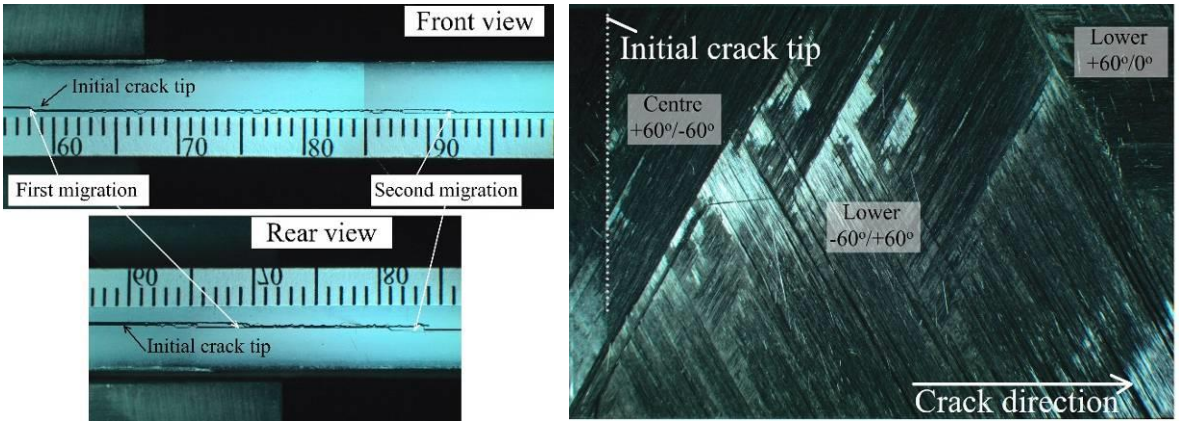

(a) Front and rear views (b) Experimental fracture surface

Fig. 11. (a) Front and rear views after the second migration event occurred and (b) Experimental fracture surface for the quasi-static specimens with θ = 60°.

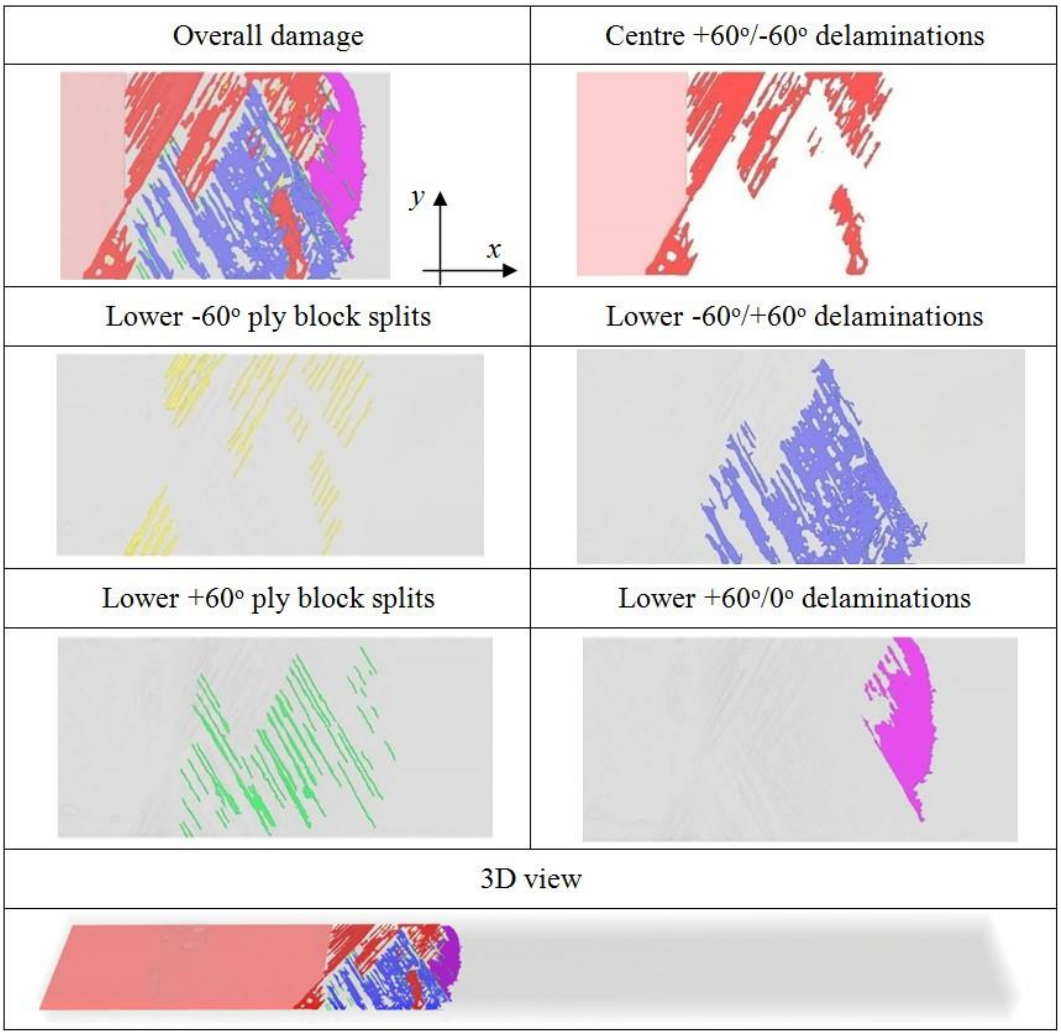

Fig. 12. CT scan of a θ=60° specimen tested quasi-statically and interrupted at stage IV (interrupted test 3)

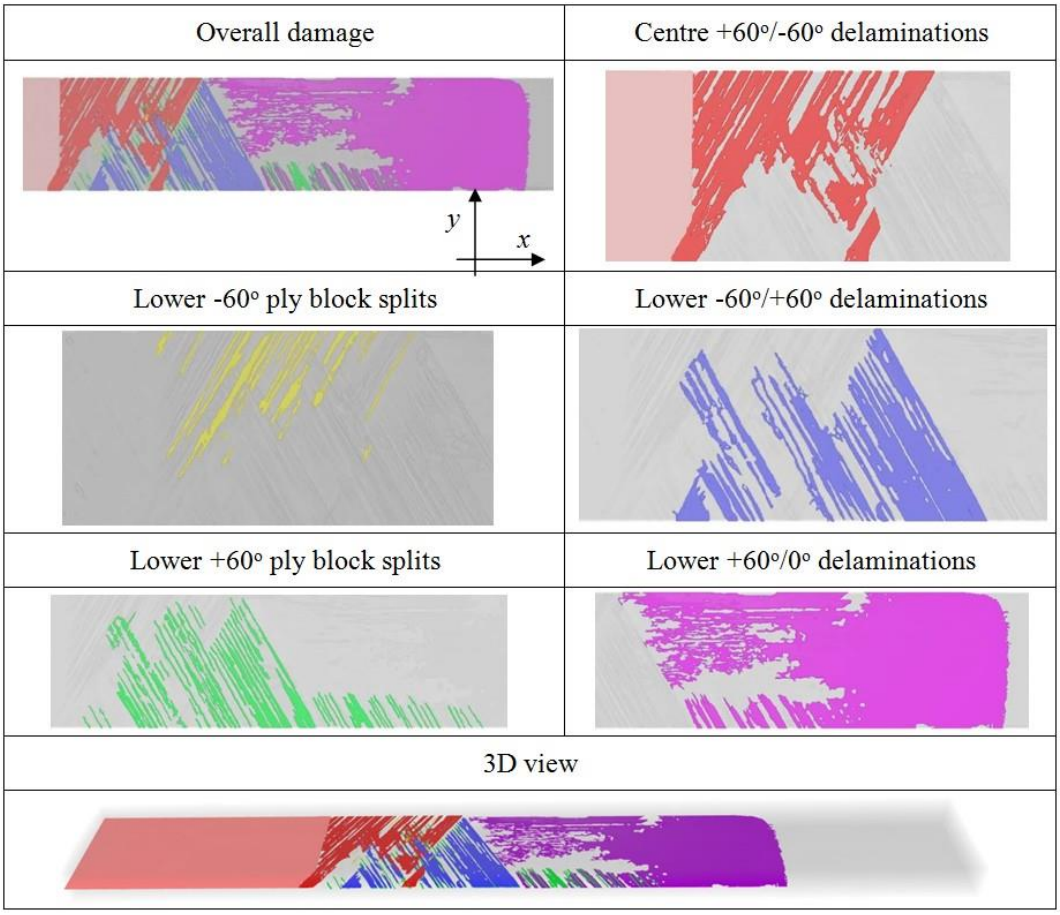

Fig. 13. CT scan of a θ=60° specimen tested quasi-statically to full failure.

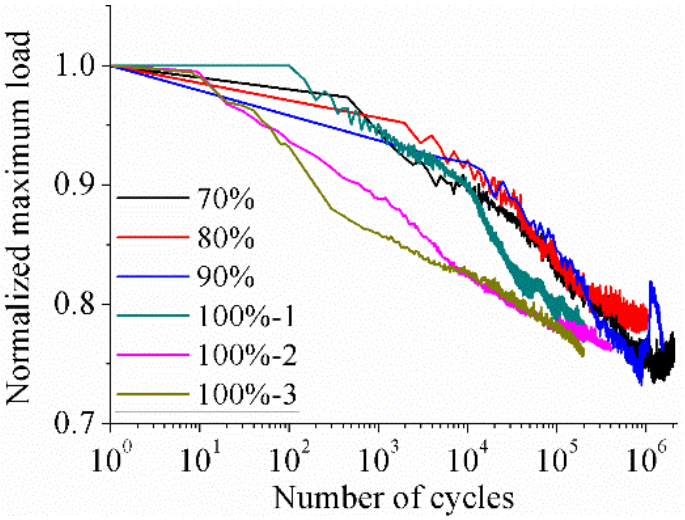

(a)

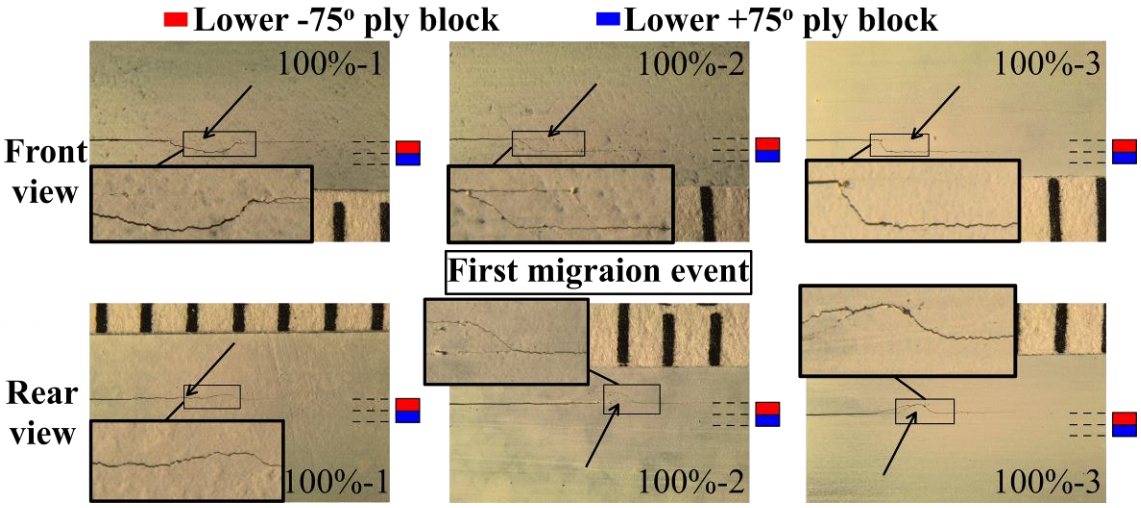

(b)

Fig. 14. (a) Initial results obtained for the fatigue tests with 60º/-60º interface and (b) edge views at different stiffness losses during the first migration event (the arrow marks the location of the initial crack tip and the scale visible is in mm).

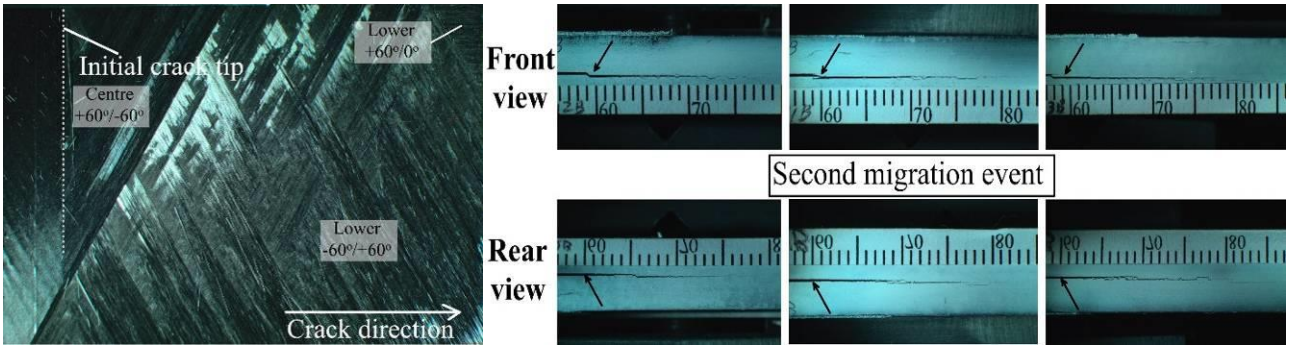

Fig. 15. Experimental fracture surface for the fatigue specimens with θ = 60° and edge views at different stiffness losses during the second migration event (the arrow marks the location of the initial crack tip and the scale visible is in mm).

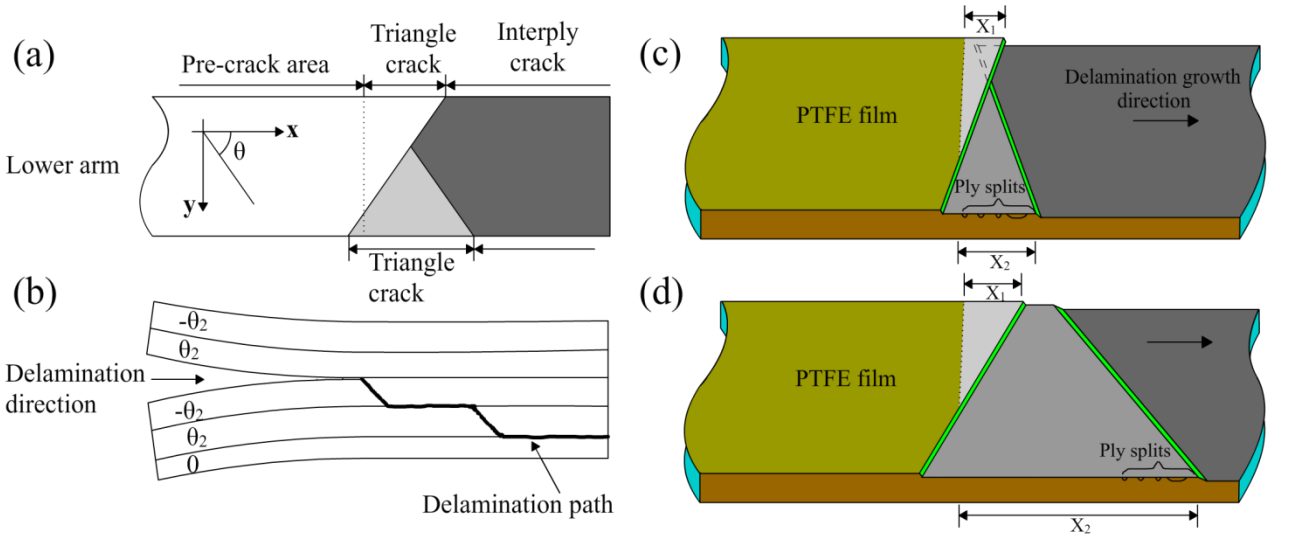

Fig. 16. Delamination shape and path: (a) top view and (b) front view; 3D sketch of fracture surface for specimen (quasi-static and fatigue) with (c) θ = 75° and (d) θ = 60°.

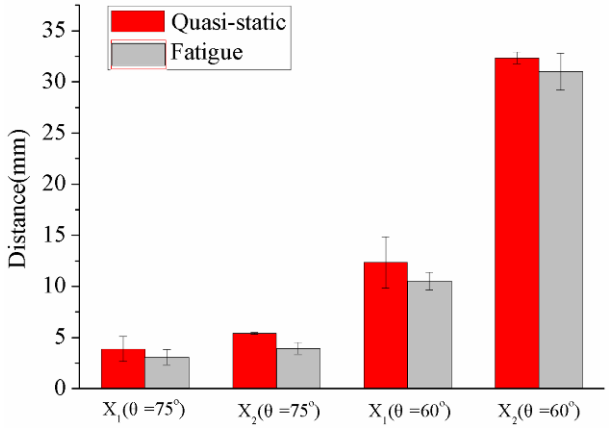

Fig. 17. Comparison of the value of X_1 and X_2 between quasi-static and fatigue specimens.

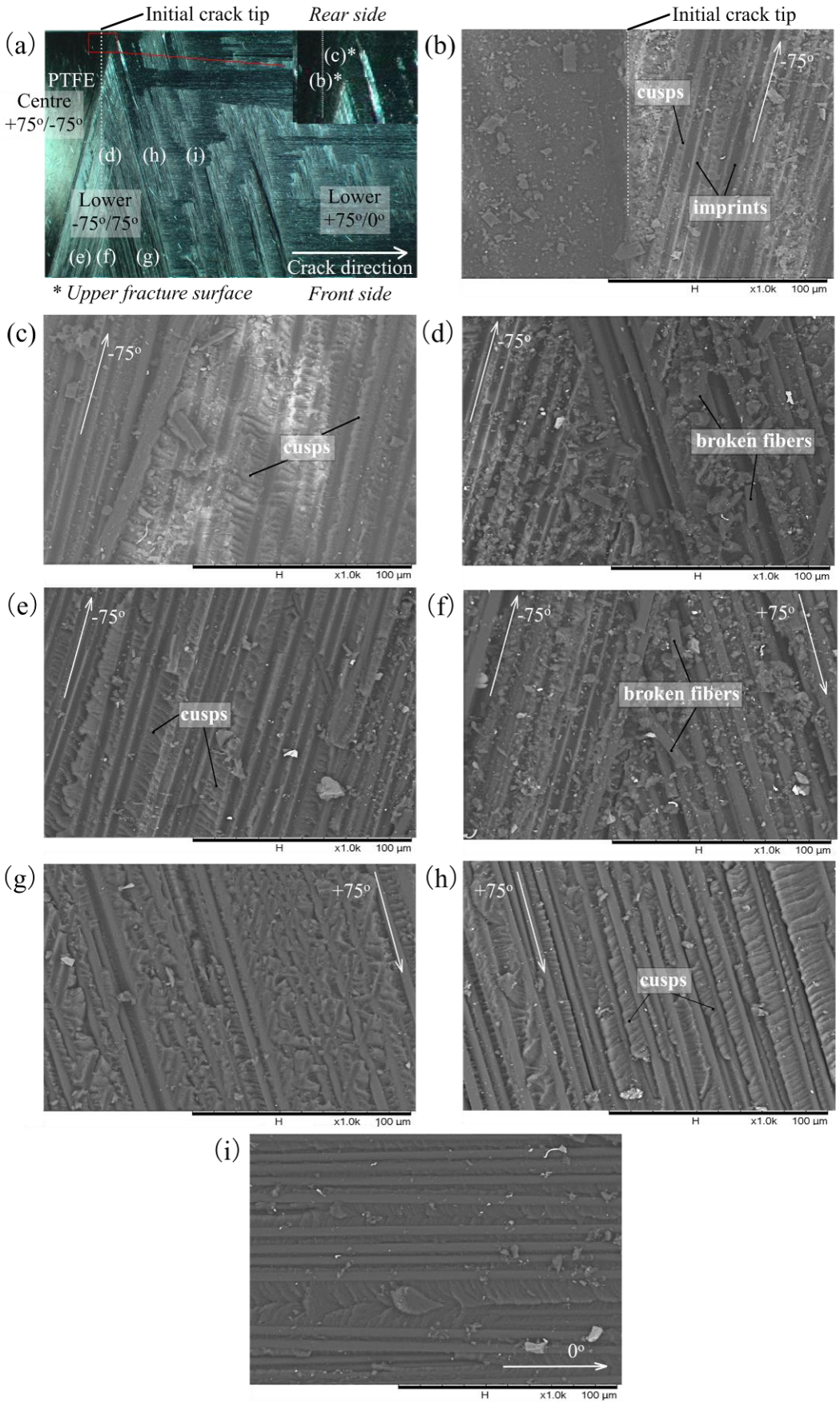

Fig. 18. Micrographs at different locations on the fracture surface from a quasi-static specimen ($\theta = 75^{o}$).

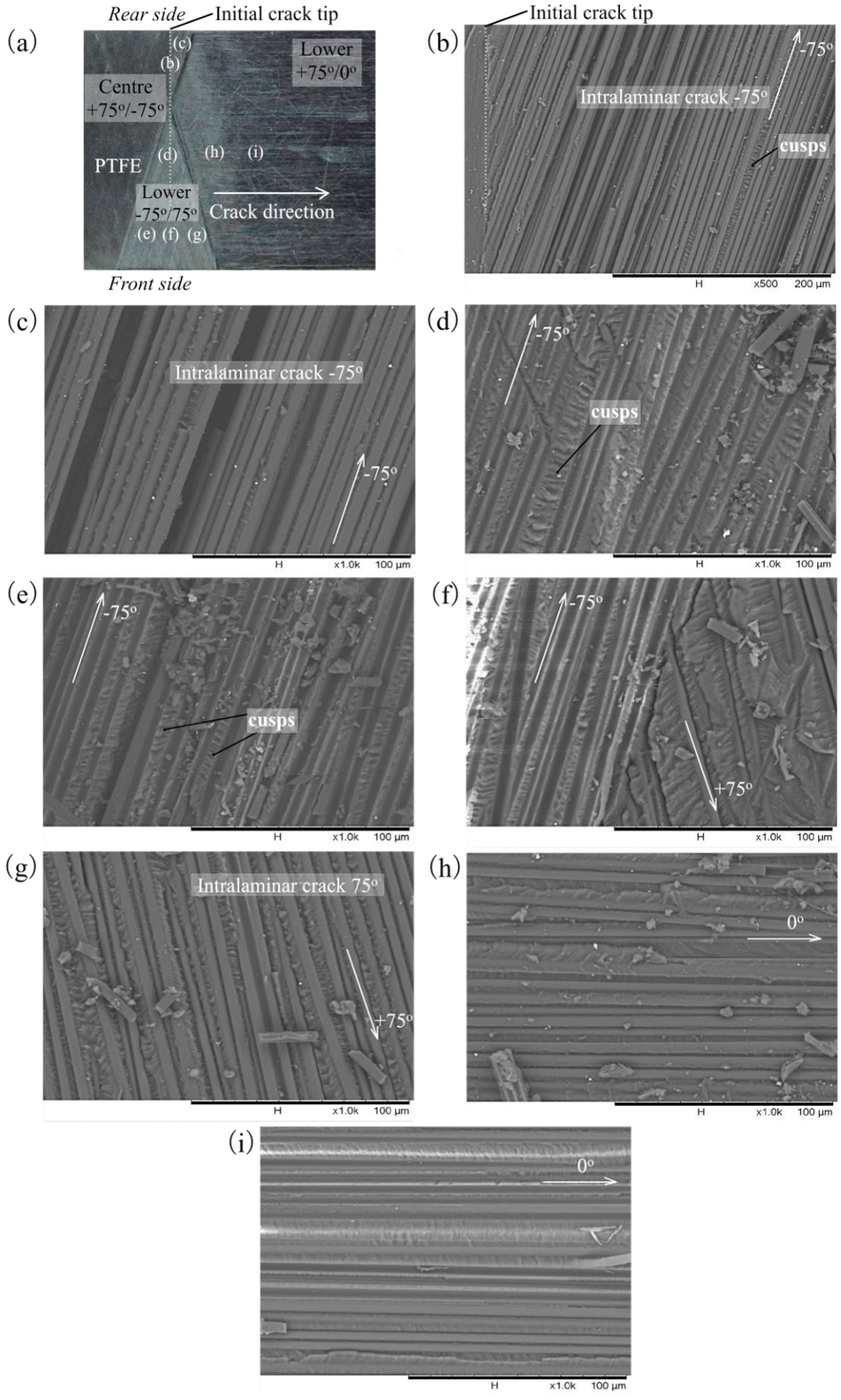

Fig. 19. Micrographs at different locations on the fracture surface from a fatigue specimen ($\theta = 75^{o}$).

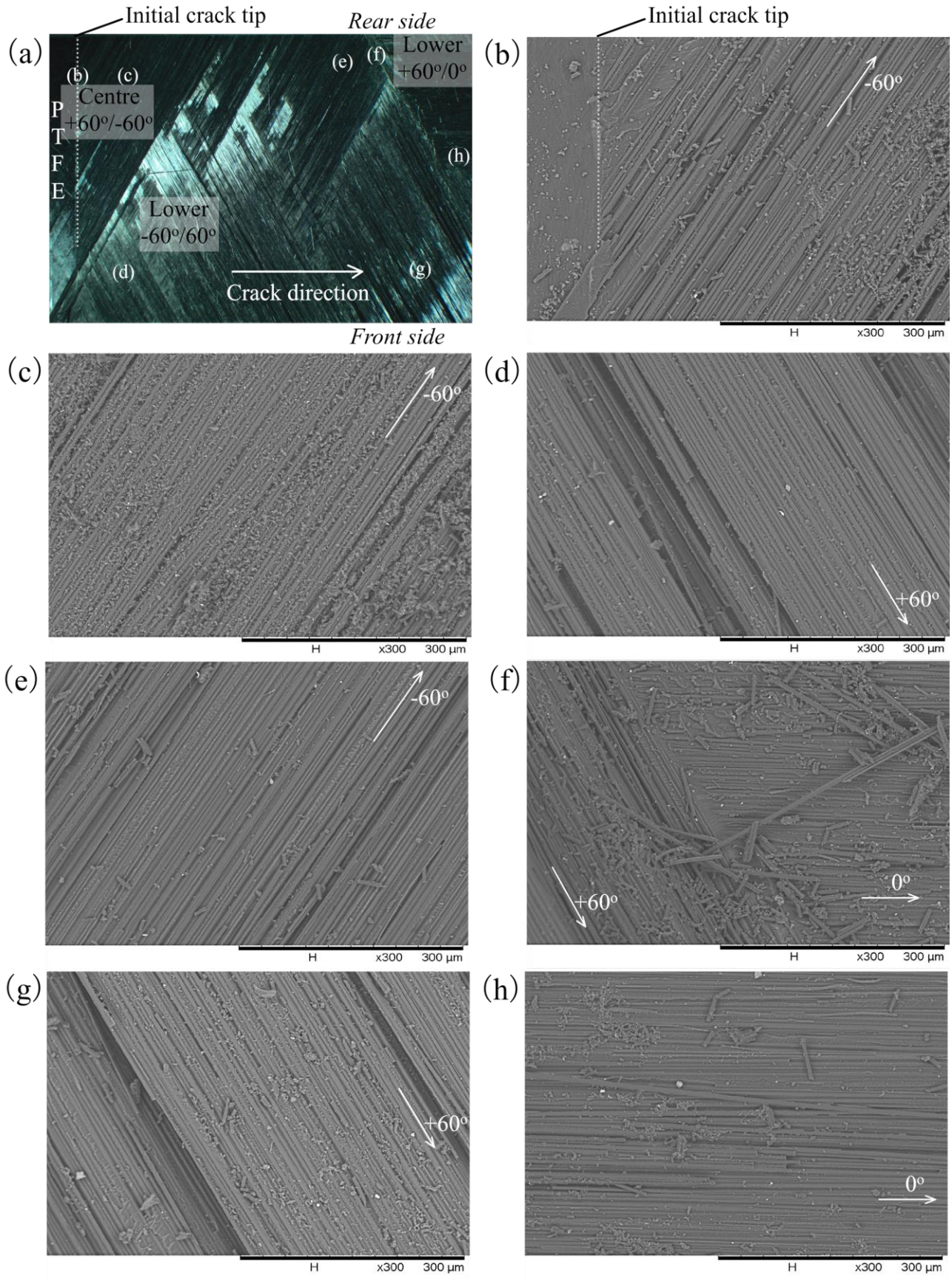

Fig. 20. Micrographs at different locations on the fracture surface from a quasi-static specimen ($\theta = 60^{o}$).

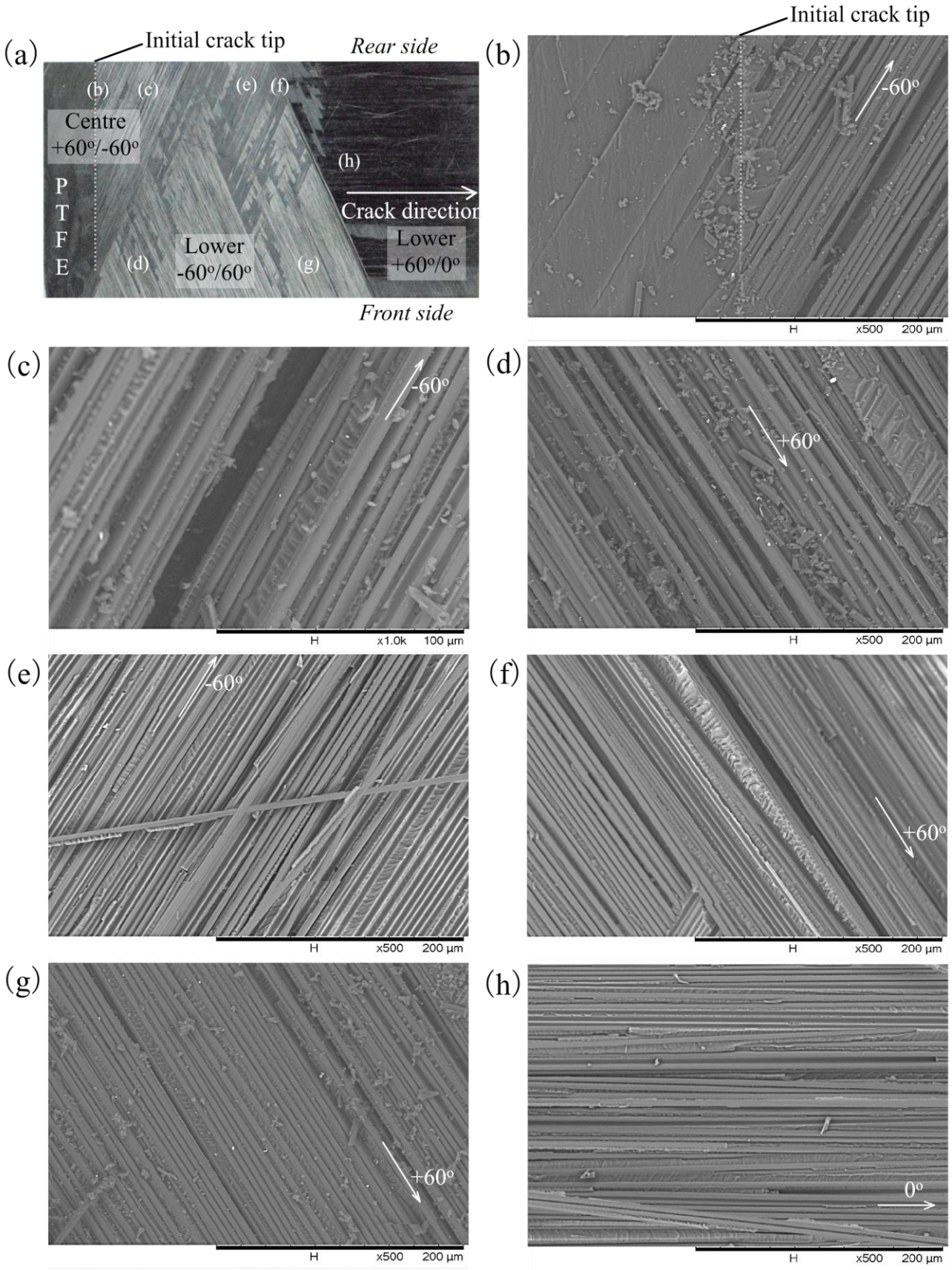

Fig. 21. Micrographs at different locations on the fracture surface from a fatigue specimen ($\theta = 60^{o}$).

Table 1 Number of specimens tested for each fibre angle, θ. Number in parenthesis indicates number of interrupted specimens.

	Quasi-static test	Severity percentages of fatigue test			
		62.5%	68.75%*	75%	100%
θ=75°	6(3)	1	3(3)	1	1
		70%	80%	90%	100%*
θ=60°	6(3)	1	1	1	3(3)

Table 2 Distances of migrated points to the PEFE insert front for quasi-static (S) and fatigue (F) specimens (Unit: mm)

θ=75°	X_1	$\bar{X}_1$ (S.D.)	X_2	$\bar{X}_2$ (S.D.)	θ=60°	X_1	$\bar{X}_1$ (S.D.)	X_2	$\bar{X}_1$ (S.D.)
S1	2.9	3.9 (1.2)	5.5	5.4 (0.1)	S1	10.0	12.3 (2.5)	32.0	32.3 (0.6)
S2	3.5		5.4		S2	15.0		33.0	
S3	5.3		5.3		S3	12.0		32.0	
F1	2.0	3.0 (0.8)	3.3	3.9 (0.6)	F1	11.0	10.5 (0.9)	29.0	31.0 (1.8)
F2	3.6		4.5		F2	11.0		32.5	
F3	3.3		3.9		F3	9.5		31.5	